Chemical Science

ROYAL SOCIETY OF CHEMISTRY

EDGE ARTICLE

View Article Online
View Journal

Cite this: DOI: 10.1039/d5sc02612a

All publication charges for this article have been paid for by the Royal Society of Chemistry

Highly efficient and selective Sr^{2+} capture using robust two-dimensional MOF nanosheets decorated with cage-like cavities†

Xiao-Ran Jia,[a] Zi-Xuan Gao,[a] Hai-Ming Fei,[c] Li-Juan Lan,[a] Cai-Xia Yu,*[a] Yong Qian*[b] and Lei-Lei Liu *[a]

Received 8th April 2025
Accepted 30th June 2025

DOI: 10.1039/d5sc02612a

rsc.li/chemical-science

The urgent need for efficient extraction of radio-strontium (Sr) from complex aquatic environments arises from its extreme radiotoxicity to both ecosystems and human health, which remains a significant challenge. In this study, we developed an ultrathin 2D **Cu-MOF-COOH** nanosheet with cage-like cavities for strontium separation. Incorporating the permanent cavity structures on the MOF nanosheet can fully utilize its structural characteristics of a largely exposed surface area and accessible adsorption sites in pollutant removal, and the comprehensive interactions between pollutants with the active sites and cavities on the exposed surfaces can achieve highly selective and efficient capture. Consequently, the **Cu-MOF-COOH** nanosheet exhibited superior capture performances, in terms of removal kinetics, selectivity, and uptake capacity, which are obviously better than its 3D counterpart. Moreover, it demonstrated ultra-high selectivity and anti-interference ability, enabling efficient Sr^{2+} removal even in the presence of large excesses of Ca^{2+}, Ba^{2+}, and other alkali and alkaline earth metal ions. Remarkable anti-interference performances were further validated by its practical applications in diverse real-world samples, including lake water, simulated groundwater, and radioactive wastewater, with Sr^{2+} removal efficiencies exceeding 91%. These exceptional extraction performances can be attributed to the synergistic interactions between the accessible active sites (carboxylate groups) and cage-like cavities with Sr^{2+}, which were clarified through a series of characterization studies and theoretical calculations. This study presents a highly promising material for the separation of radioactive Sr^{2+} from aqueous solution and, more importantly, offers a novel strategy for the rational design of ultrathin MOF nanosheets with cavity structures, which holds great potential for expanding the applications of MOF nanosheets.

Introduction

With the growing concerns over the energy crisis and climate change, nuclear power emerged as a promising alternative to fossil fuels.[1] The safe management of radioactive wastes produced by nuclear power plants entails considerable difficulties. Among these, strontium-90 (^{90}Sr) stands out as a particularly problematic radioisotope due to its relatively long half-life ($t_{1/2}$ = 28.80 years) and high-energy β-emission (0.546 MeV).[2,3] Moreover, the large inventory, high environmental mobility, and extremely high radiotoxicity made ^{90}Sr one of the primary environmental concerns.[4] Detailed radioecological investigations on the Chernobyl accident revealed the ultra-high mobility of radio-strontium in water bodies, where it exists in the form of Sr^{2+}.[5,6] Besides, due to its similar chemical characteristics to Ca^{2+}, Sr^{2+} can be readily combined with bones, ultimately leading to bone cancers and leukemia.[7,8] As a consequence, it is urgent to develop an efficient and targeted method for the separation of ^{90}Sr from aqueous solutions.

Metal–organic frameworks (MOFs) are a class of crystalline hybrid materials formed through the intricate coordination of metal ions or clusters with organic ligands.[9–12] Due to their rationally designed and systematically adjustable structures and chemical functionalities, MOFs can be tailored to trap target pollutants within their pre-organized pores, with specific capture sites.[13–17] Therefore, MOFs have emerged as advanced solid materials for efficient remediation of various environmental pollutants, including small-molecule organic pollutants,[18,19] dyes,[20] heavy metal ions,[21,22] and radioisotopes.[23–26] To date, numerous MOFs have been developed for Sr^{2+} separation,

[a]School of Environmental and Material Engineering, Yantai University, Yantai 264005, P. R. China. E-mail: liuleileimail@163.com

[b]State Key Laboratory of Nuclear Resources and Environment, East China University of Technology, Nanchang, Jiangxi 330013, P. R. China

[c]College of Chemical Engineering, Huaqiao University, Xiamen 361021, P. R. China

† Electronic supplementary information (ESI) available: Materials and physical measurements, extraction experiments, calculation method, particle size distribution, elemental mapping images, PXRD patterns, FT-IR spectra, TGA curves, SAED patterns, contact angle, zeta potentials, and additional figures, tables and an X-ray crystallographic file in CIF format. CCDC 2427696. For ESI and crystallographic data in CIF or other electronic format see DOI: https://doi.org/10.1039/d5sc02612a

with several exhibiting high uptake capacities and selectivity. Yuan and Wang *et al.* synthesized a novel MOF-18Cr6, which held regular cavities and demonstrated selective separation of Sr^{2+} with a maximum uptake capacity of 84.93 mg g^{-1}.[27] Xiao and co-workers incorporated 18-crown-6 and 24-crown-8 into a Zr-MOF, resulting in a material that exhibited rapid adsorption kinetics and a high adsorption capacity for Sr^{2+} (149 mg g^{-1}).[8] Recently, Shi and Mei *et al.* designed and synthesized acyl-anchored metal–organic cages with interior cryptand-like recognition sites, which achieved highly selective removal of trace Sr^{2+}.[28] Park *et al.* constructed an anionic MOF and adopted the ion-exchange method for selective capture of Sr^{2+} from wastewater, achieving an adsorption capacity of 41.1 mg g^{-1}.[3] Despite the tunable nature and periodic structure, which conferred efficient extraction performance in Sr^{2+} removal, the limited diffusion rate and accessibility to the active sites embedded within the bulky framework significantly impaired the adsorption performances of most 3D MOFs, including their adsorption kinetics, selectivity, and uptake capacities. In particular, selectivity, along with the corresponding anti-interference capability, is a crucial factor for the application of MOF materials in complex practical water samples. Although MOFs can be purposefully modified with specific functional groups to enhance the selectivity for target removal, and this approach does yield some positive results,[29,30] the indirect interaction between the binding sites in bulk MOFs with pollutants, primarily driven by electrostatic forces that initially attract the pollutants into the pores, significantly reduces the capture selectivity.[31] And it still remains a significant challenge to separate Sr^{2+} from complicated systems that contain alkali and alkaline earth metal ions with similar electronic structures and chemical properties.[32]

To address the limitation of the restricted access to the internal sites within three-dimensional (3D) MOFs, 2D MOF nanosheets, characterized by their adequately exposed surfaces and active sites, have been successfully synthesized.[33] The highly open structure of MOF nanosheets allows for the exposure of more accessible active sites, which would facilitate intimate contact and adequate interactions with pollutant molecules on the exposed surfaces, leading to enhanced selectivity and uptake capacities.[34–37] Despite the numerous structural advantages in pollutant capture, the exfoliated nanosheets lack the necessary containers or cavities to accommodate pollutants, which is beneficial for the stable capture of pollutants.[38,39] To fully utilize the unique structural advantages of 2D MOF nanosheets in pollutant removal, functionalizing pores or cavities onto their surfaces could be an effective strategy, which would not only maintain the accessibility of active sites but also provide the necessary space for pre-enriching and accommodating pollutant molecules, thereby enhancing the overall performance of the material in pollutant removal.

Calix[*n*]arenes (n = 4, 6, and 8), with a special cup-shaped structure and easily modified rims, can be an ideal ligand for the construction of MOF nanosheets with cavity structures.[40–42] Herein, the calix[4]arene of 5,11,17,23-tetra-*tert*-butyl-25,26,27,28-tetrakis[(carboxyl)methoxy]calix[4]arene (H_4L; Scheme S1†), functionalized with carboxyl groups and *tert*-butyl groups, was selected for the fabrication of MOFs for Sr^{2+} separation. In the design, the ligand H_4L was modified with four carboxyl groups on the lower rims, which would be facile for the construction of cage-like cavities by the connection with metal ions, and the left uncoordinated carboxyl groups in the cavity can serve as Sr^{2+} capture sites (Scheme 1); the upper rims of H_4L were modified with four *tert*-butyl groups, which generally do not get involved in MOF construction, thus their space hindered effect is conducive to obtaining a layered structure. The large spatial dimensions of the *tert*-butyl groups are anticipated to endow the resulting MOFs with large interlayer distances, facilitating their efficient exfoliation into ultrathin nanosheets.[43] Additionally, the *tert*-butyl groups on the 2D surfaces can prevent the nanosheets from stacking, which indirectly increases the available interaction area for Sr^{2+} extraction.

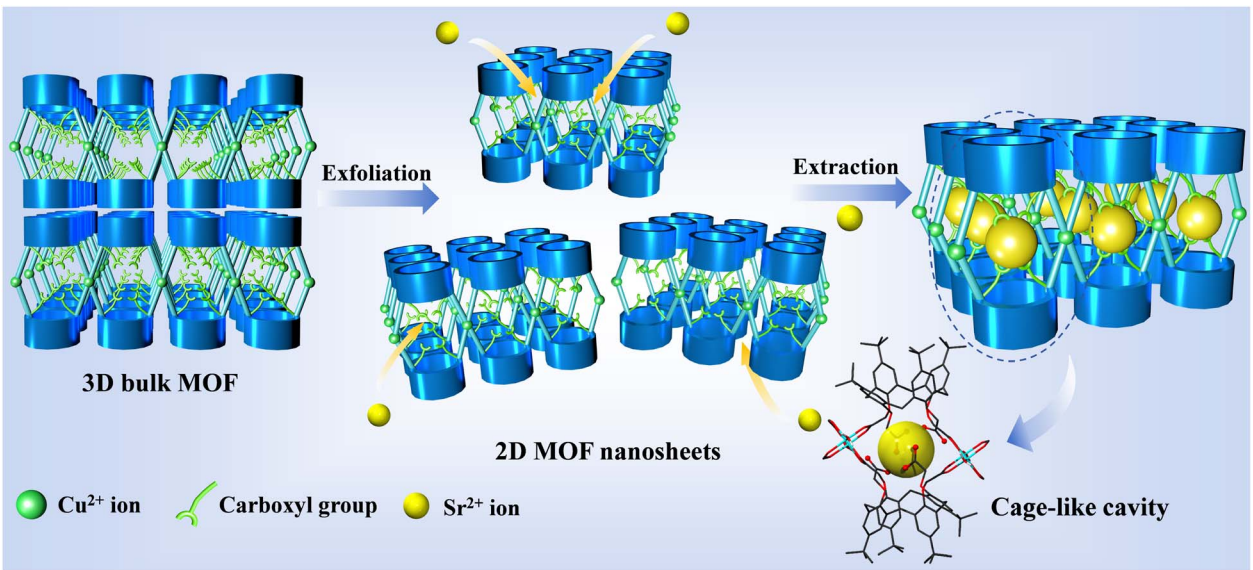

Scheme 1 Construction strategy diagram of 2D Cu-MOF-COOH nanosheets for selective Sr^{2+} capture.

Moreover, the excellent hydrophobic properties of these *tert*-butyl groups, which were decorated on the exfoliated MOF nanosheets, would endow MOF nanosheets with high stability in aqueous solution, even under harsh conditions of strong acids or bases. Thus, the solvothermal reaction of $CuCl_2 \cdot 2H_2O$ with H_4L generated a MOF with a layered structure, $\{[Cu(H_2L)(H_2O)] \cdot 0.5H_2O\}_n$ (**Cu-MOF-COOH**), which can be readily delaminated into an ultrathin nanosheet with cavity structures by a straightforward ultrasonic method (Scheme 1). As anticipated, the synergistic interaction between the extensively accessible adsorption sites (carboxylate groups) and the cage-like cavities with Sr^{2+} on the exposed surfaces resulted in exceptional capture performance for Sr^{2+}, with high removal efficiencies (>91%) from various water samples.

Results and discussion

Characterization of Cu-MOF-COOH

Single-crystal X-ray crystallographic analysis reveals the crystallization of **Cu-MOF-COOH** in the monoclinic space group $P2_1/c$. Fig. S1† illustrates that two $Cu(H_2O)$ subunits are connected by four carboxylate groups to form a paddle-wheel unit, $[Cu_2(COO)_4(H_2O)_2]$. Two paddle-wheel units are then linked through two H_2L^{2-} ligands, resulting in cage-like secondary building units (Fig. 1a). These units are interconnected to create a 2D layered structure (Fig. 1b and c), which are further stacked together to form a 3D structure (Fig. 1d). Notably, the upper rims of the H_4L ligand are modified with four *tert*-butyl groups, with large spatial dimensions, which impart the resulting layered MOFs with substantial interlayer distances (Fig. 1d), thereby facilitating their efficient exfoliation into ultrathin nanosheets. The cage-like cavities on the largely exposed surface are filled with extensive and accessible uncoordinated carboxylate O atoms (Fig. 1a and b), allowing for easy interaction with Sr^{2+} that facilitates efficient and selective separation. Notably, within the cavities, the oxygen atoms of carboxylate groups at *ortho*-positions are capable of coordinating with Sr^{2+} through a bidentate chelating mode. The oxygen–oxygen distances are measured to be 5.210 Å and 5.213 Å (Fig. S2†), which are comparable to that of a previous study,[28] where an oxygen–oxygen distance of approximately 5.18 Å is optimal for Sr^{2+} capture. These distances are well-suited for Sr^{2+} capture, due to the size-matching effect.[28] The cage-like cavities would play a pivotal role in the interactions between Sr^{2+} and the O sites, and the synergistic interactions between the accessible active sites and cage-like cavities with Sr^{2+} would ensure stable capture of Sr^{2+}, overcoming the problem of conventional 2D materials' easy desorption.

Exfoliation of Cu-MOF-COOH

Given the large interlayer spacing and weak interactions between the layers in **Cu-MOF-COOH**, a liquid-based

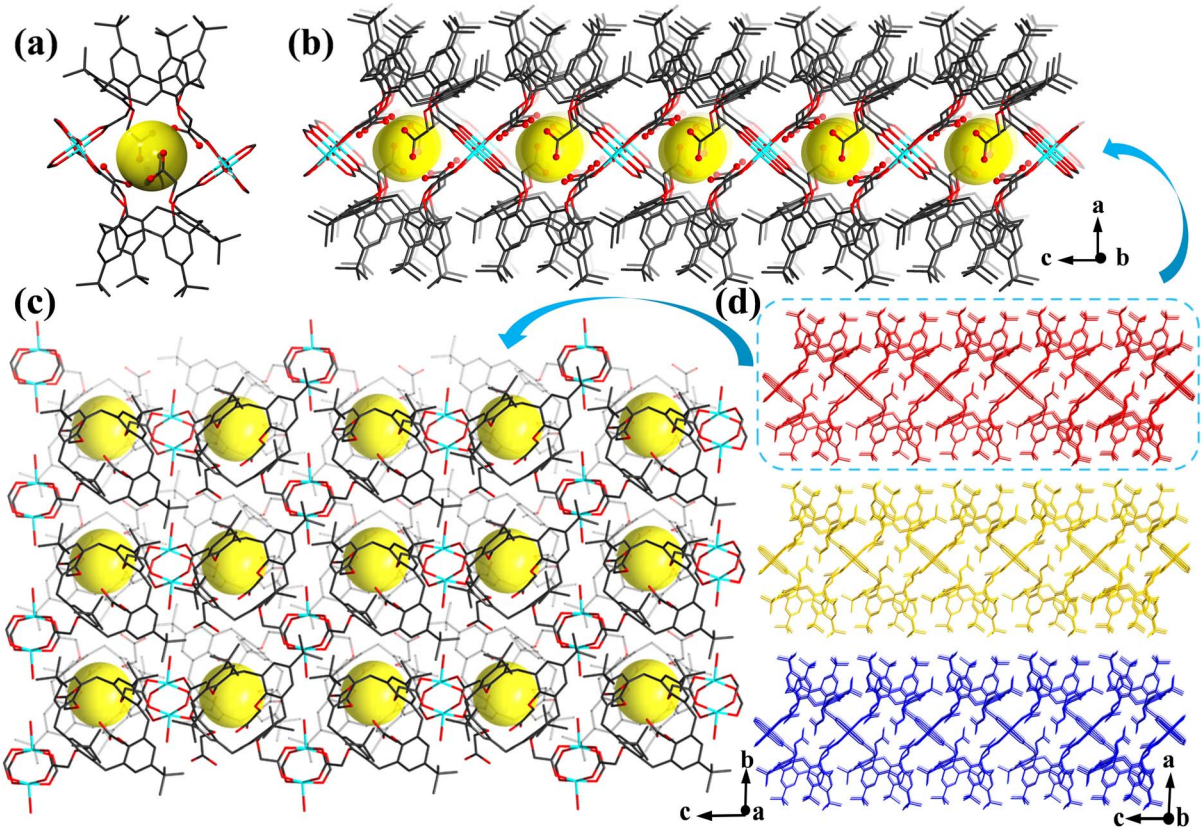

Fig. 1 (a) View of the cage-like secondary building unit in **Cu-MOF-COOH**. Atom color codes: cyan, Cu; red, O; dark gray, C. (b and c) View of the 2D structures in **Cu-MOF-COOH**. (d) The 3D structure of **Cu-MOF-COOH**.

ultrasonication approach was utilized to exfoliate the bulk MOF. By immersing it in MeOH/isopropanol solution and subjecting it to ultrasonication for 6 h, a colloidal suspension was formed. Upon illumination with a red laser, a noticeable Tyndall effect can be observed (inset in Fig. 2d), indicating the successful exfoliation into 2D **Cu-MOF-COOH** nanosheets, which was further validated by the particle size distribution analysis of dynamic light scattering. As shown in Fig. S3,† the obtained nanosheets exhibit an average dimension of 187 nm after exfoliation. A series of measurements, encompassing scanning electron microscopy (SEM), transmission electron microscopy (TEM), and atomic force microscopy (AFM), were conducted to scrutinize the morphology of the resultant MOF nanosheets. SEM images clearly showed the transformation of the square-shaped bulk **Cu-MOF-COOH** (Fig. 2a) into flake-like 2D **Cu-MOF-COOH** nanosheets (Fig. 2b and c). Notably, some **Cu-MOF-COOH** nanosheets exhibited curling, due to their ultrathin nature, which was further confirmed by the TEM image shown in Fig. 2d. AFM measurements provided detailed information on the thickness of **Cu-MOF-COOH** nanosheets, revealing an approximate thickness of 6.25 nm (Fig. 2e and f), which consisted of about 3 layers. The aforementioned findings verified that **Cu-MOF-COOH** was successfully exfoliated into ultrathin nanosheets. Moreover, the element mappings of **Cu-MOF-COOH** nanosheets (Fig. S4†) revealed a uniform distribution of Cu, C, and O elements throughout the nanosheets.

To further confirm the successful exfoliation of 2D nanosheets, the powder X-ray diffraction (PXRD) measurements were performed. Fig. S5† shows the PXRD patterns of 3D **Cu-MOF-COOH** and **Cu-MOF-COOH** nanosheets. It is obvious that the diffraction pattern of 3D **Cu-MOF-COOH** exhibited a strong diffraction peak at 3.90°, corresponding to the (100) facet, which indicated that periodic stacking formed along the *a* axis in 3D **Cu-MOF-COOH**. After exfoliation, the peak at 3.90° (100) clearly displayed a slight shift to 3.80°, indicating the expansion of the interlayer spacing. Moreover, the peak at 3.80° (100) was broadened, and its intensity was significantly reduced compared to that of its 3D bulk counterpart (inset in Fig. S5†), which further confirmed that the nanosheets were exfoliated along the *a*-axis direction.[44,45] Fourier transform infrared (FT-IR) spectroscopy and thermogravimetric analysis (TGA) were conducted to investigate the integrity of the framework after exfoliation. The curves of these measurements for **Cu-MOF-COOH** nanosheets were found to be almost identical to those of their 3D counterparts (Fig. S6 and S7†), confirming that the framework structure remained intact after exfoliation. The clear diffraction spots in the selected area electron diffraction (SAED) image (Fig. S8†) further indicated that the 2D nanosheets retained their crystallinity after exfoliation.

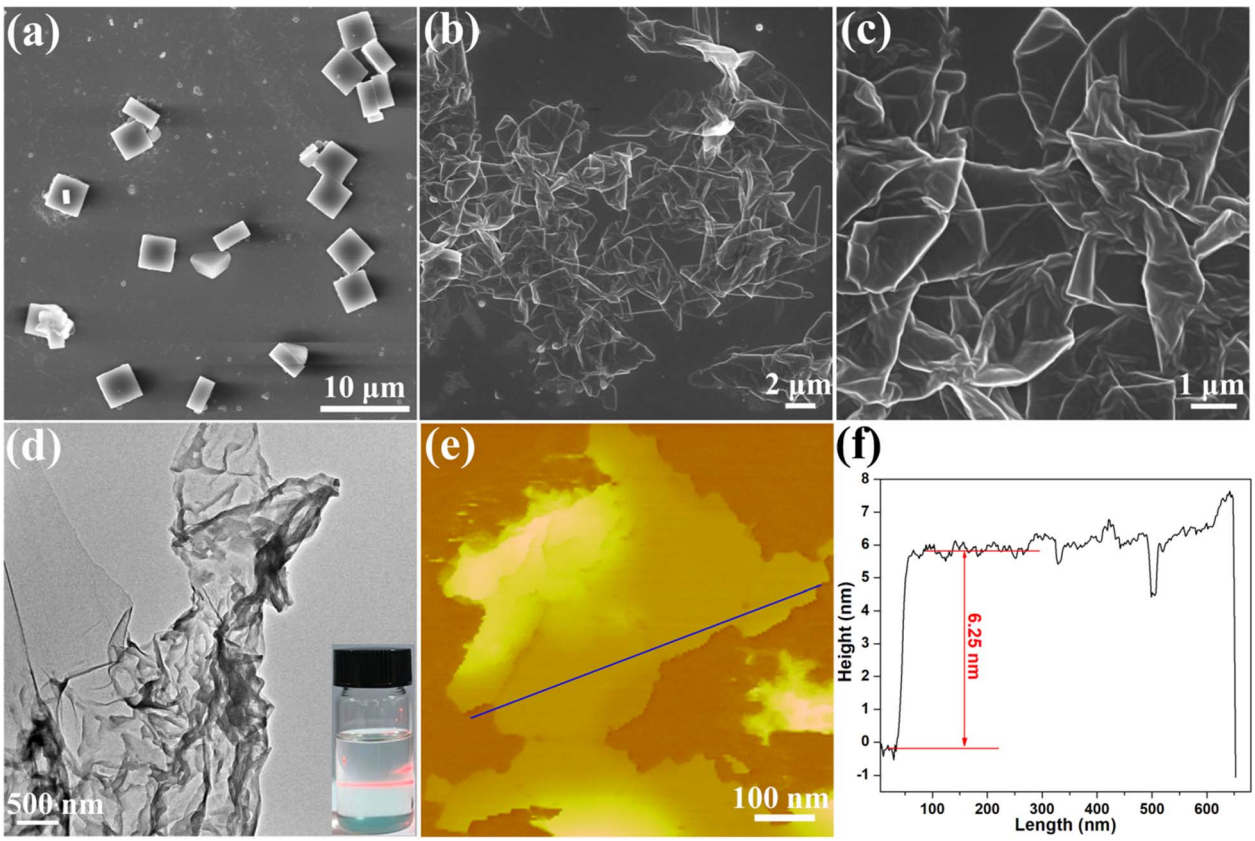

Fig. 2 (a) SEM image of the square-shaped bulk **Cu-MOF-COOH**. (b and c) SEM images of **Cu-MOF-COOH** nanosheets. (d) TEM image of **Cu-MOF-COOH** nanosheets; inset: photograph of the Tyndall effect of **Cu-MOF-COOH** nanosheet suspension. (e) AFM image of **Cu-MOF-COOH** nanosheets. (f) Height profile, color-coded blue, is measured along the corresponding track shown in (e).

The water stability of **Cu-MOF-COOH** nanosheets was also investigated by immersing them in aqueous solutions with varied pH values. After immersing in aqueous solution at pH of 1.0, 2.0, 3.0, 5.0, 7.0, 9.0, 10.0, 12.0 and 13.0 for 12 hours, only 2.16%, 1.31%, 0.27%, 0.13%, 0.01%, 0.09% 0.06%, 0.73% and 3.31% Cu^{2+} leaching was determined (Table S1†), respectively. Moreover, the acquired PXRD patterns matched those of the original ones well (Fig. S9†), demonstrating the remarkable stability of **Cu-MOF-COOH** nanosheets, even under extremely acidic and alkaline conditions. This robustness can be attributed to the abundant hydrophobic *tert*-butyl functional groups decorated on the MOFs, which impart a high degree of hydrophobicity to **Cu-MOF-COOH** nanosheets, as evidenced by their high contact angle (130.4°; Fig. S10†). This hydrophobicity can prevent water molecules from attacking the central metal ions, enhancing the chemical stability of the MOF nanosheets. These results demonstrate the high water stability of **Cu-MOF-COOH** nanosheets, which is essential for their application in Sr^{2+} separation from actual water samples.

Sr^{2+} capture studies

The pH value is a crucial element controlling the uptake of an adsorbent by affecting the surface charge of adsorbents and the type of metal ions in the solution. Thus, it is essential to investigate the influence of pH on Sr^{2+} extraction. Given the formation of Sr^{2+} hydroxide precipitates under alkaline conditions, we investigated Sr^{2+} extraction behavior within a pH range from 3.0 to 10.0. As shown in Fig. 3a, at a pH of 3.0, the extraction efficiency of Sr^{2+} was only 26.46%, which can be attributed to the competition between Sr^{2+} with the excess H^+ in the solution. As pH increased, the removal efficiency for Sr^{2+} improved significantly, reaching a peak value of 99.34% at pH 10.0. This enhancement can be attributed to the deprotonation of carboxyl groups in **Cu-MOF-COOH** nanosheets under weak alkaline conditions, favouring Sr^{2+} removal through electrostatic interactions, and it was supported by zeta potential analyses of **Cu-MOF-COOH** nanosheets at different pH levels (Fig. S11†). As pH increases from 3.0 to 10.0, the increase in surface charge enhances the electrostatic attraction with Sr^{2+}, thereby improving Sr^{2+} removal. Thus, a pH of 10.0 was selected as the optimal pH for further investigation.

The rapid sequestration of radioactive elements serves as an effective strategy to mitigate radiation risks. To this end, the kinetic properties of **Cu-MOF-COOH** nanosheets were evaluated in Sr^{2+} solution at a concentration of 5 ppm. As illustrated in Fig. 3b, **Cu-MOF-COOH** nanosheets exhibited a relatively rapid kinetics for Sr^{2+}, achieving an extraction efficiency of 83.88% within the first minute. The extraction gradually approached equilibrium, ultimately reaching a removal efficiency of 99.56%. Under the same experimental conditions, 3D **Cu-MOF-COOH** removed only 39.05% of Sr^{2+} within the initial minute and ultimately achieved a removal efficiency of 82.09% (Fig. 3b). The significant difference in the removal rates between 2D and 3D MOFs during the initial stage is primarily attributed to the accessibility of the contaminants to the adsorption sites on extractants. The abundant active sites on the surface of **Cu-MOF-COOH** nanosheets, which are readily accessible, provide numerous opportunities for Sr^{2+} to interact with the binding sites, ultimately leading to a significantly higher removal efficiency within a short period. For 3D **Cu-MOF-COOH**, the high density of active sites confined within the framework resulted in diminished Sr^{2+} capture performance. To examine the rate-controlling mechanisms of these extraction processes, pseudo-first-order and pseudo-second-order kinetic models were employed to fit the data for both **Cu-MOF-COOH** nanosheets and 3D **Cu-MOF-COOH** (Fig. S12†). As illustrated in Table S2,† the pseudo-second-order kinetic model with higher R^2 values (0.999 and 0.998) can better fit the data of both 2D and 3D **Cu-MOF-COOH**, demonstrating that the extraction process is primarily governed by chemical interactions.

To examine the maximum capture capacities for Sr^{2+}, the extraction experiments were conducted in Sr^{2+} solutions with different initial concentrations. As illustrated in Fig. 3c, the trapping capacities of **Cu-MOF-COOH** nanosheets increased with rising Sr^{2+} concentrations, ultimately reaching a maximum value of 231.72 mg g^{-1}, which was much higher than that of most materials (Table S3†). To gain further insights into the extraction process, the experimental data were fitted with both the Langmuir and Freundlich models (Fig. S13†). The fitting results, presented in Table S4,† revealed that the Langmuir model, with a higher correlation coefficient ($R^2 = 0.999$), was more suitable for describing the isotherm data of the MOF nanosheets. The calculated maximum value, 257.07 mg g^{-1}, was close to the experimentally determined value (231.72 mg g^{-1}). As a comparison, the extraction behavior of 3D bulk **Cu-MOF-COOH** was also investigated, and the equilibrium extraction capacity was determined to be 147.79 mg g^{-1}, significantly lower than that of 2D **Cu-MOF-COOH** nanosheets. This observation is in line with our predictions, as the bulk **Cu-MOF-COOH** encapsulates a substantial quantity of capture sites within its internal structure, which poses a considerable hindrance to the effective interaction with Sr^{2+}. These findings highlighted the significant improvement in contaminant accessibility to the active sites within MOF cavities through exfoliation, and the contaminant molecules can be stably captured by sufficient interaction with these active sites.

Wastewaters generally contain various alkali and alkaline earth metal ions such as Na^+, K^+, Rb^+, Cs^+, Mg^{2+}, Ca^{2+}, Ba^{2+}, *etc.*, with similar electronic structures and chemical properties to Sr^{2+}, which may compete for binding sites with Sr^{2+}.[46] Therefore, it is necessary to evaluate the selectivity and anti-interference performance of **Cu-MOF-COOH** nanosheets in the presence of these metal ions. Selective extraction experiments were conducted by adding the extractants to single metal ion solutions (Na^+, K^+, Rb^+, Cs^+, Mg^{2+}, Ca^{2+}, Ba^{2+} and Sr^{2+}), with a concentration of 10 ppm. As shown in Fig. 3d, the MOF nanosheets exhibited distinct selectivity for Sr^{2+}, with a removal ratio of up to 99.34%, which far exceeded that of other ions. For Ca^{2+} and Ba^{2+}, which have quite similar physicochemical properties to Sr^{2+}, their removal efficiencies were only 9.98% and 25.97%, respectively. And for other alkali and alkaline earth metal ions, their removal efficiencies were notably lower, falling below 2.23%. The above results demonstrated the ultrahigh

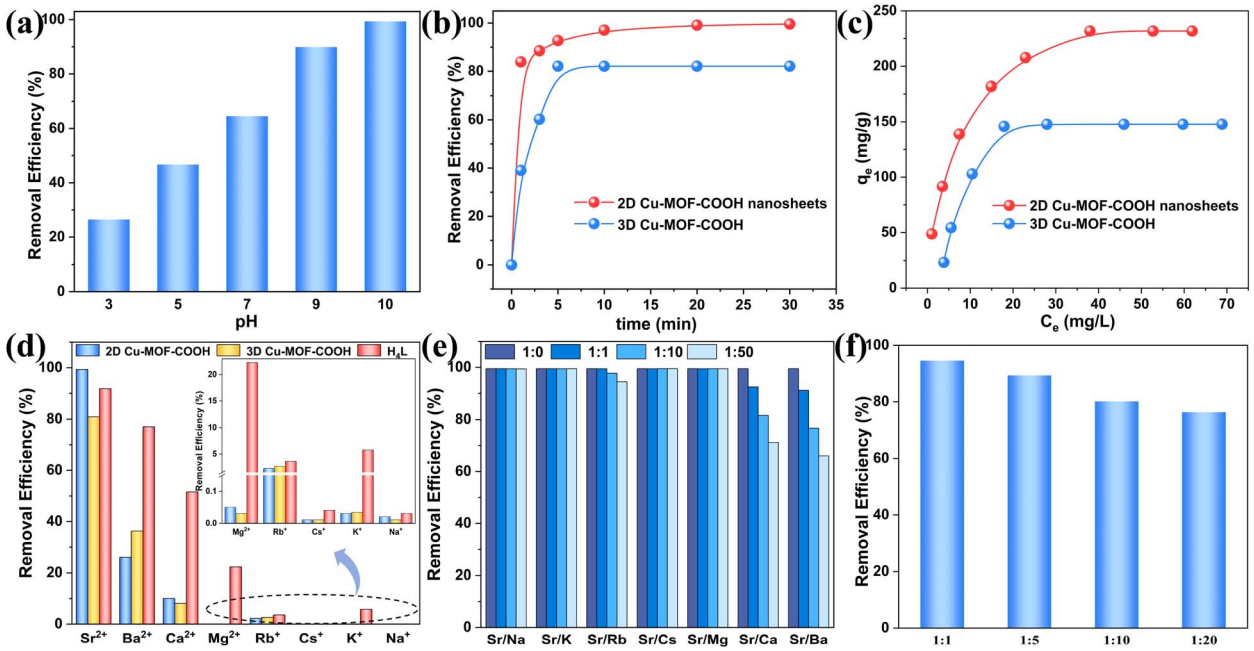

Fig. 3 (a) Impact of pH on the removal of Sr^{2+} by **Cu-MOF-COOH** nanosheets ($V_{toluene}/V_{aqueous\ phase}$ = 10 mL/15 mL, m V^{-1} = 0.7 mg mL^{-1}). (b) Sr^{2+} removal efficiency of bulk **Cu-MOF-COOH** and **Cu-MOF-COOH** nanosheets at different contact times (pH = 10.0, $V_{toluene}/V_{aqueous\ phase}$ = 10 mL/15 mL, m V^{-1} = 0.7 mg mL^{-1}). (c) Isotherm of Sr^{2+} capture by bulk **Cu-MOF-COOH** and **Cu-MOF-COOH** nanosheets (pH = 10.0, $V_{toluene}/V_{aqueous\ phase}$ = 10 mL/60 mL, m V^{-1} = 0.5 mg mL^{-1}). (d) Selectivity of **Cu-MOF-COOH** nanosheets, 3D bulk **Cu-MOF-COOH** and H_4L ligands for different metal ions (pH = 10.0, $V_{toluene}/V_{aqueous\ phase}$ = 10 mL/15 mL, m V^{-1} = 0.7 mg mL^{-1}). (e) Influence of coexisting metal ions on the removal of Sr^{2+} by **Cu-MOF-COOH** nanosheets (pH = 8.0, $V_{toluene}/V_{aqueous\ phase}$ = 10 mL/15 mL, m V^{-1} = 0.7 mg mL^{-1}). (f) The selectivity of **Cu-MOF-COOH** nanosheets towards Sr^{2+} in a mixture of metal ions (pH = 8.0, $V_{toluene}/V_{aqueous\ phase}$ = 10 mL/15 mL, m V^{-1} = 3 mg mL^{-1}). Note: the pH value employed in the investigations depicted in (e) and (f) was set at 8.0, because some metal ions tend to precipitate at a pH of 10.0, particularly when present at high concentrations.

selectivity of **Cu-MOF-COOH** nanosheets, which can be attributed to the synergistic interaction between the accessible active sites and the cage-like cavities with Sr^{2+} on the exposed surfaces. To verify our conjecture, the selective extraction performances for bulk **Cu-MOF-COOH** and H_4L ligands were further investigated under the same experimental conditions. As shown in Fig. 3d, bulk **Cu-MOF-COOH**, with a large number of carboxylate groups and cavity structure that were buried in the framework, showed a much lower selectivity and removal rate (80.92%) for Sr^{2+} compared to that of **Cu-MOF-COOH** nanosheets (99.34%). The H_4L ligand, with sufficient –COOH groups but without a suitable cavity structure, demonstrated a certain trapping ability for most metal ions except Na^+ and Cs^+, resulting in much lower selectivity for Sr^{2+}. Therefore, the unique structure of **Cu-MOF-COOH** nanosheets, which features numerous cage-like cavities on their exposed surfaces and each cavity contains several active sites, can be responsible for the remarkable selectivity for Sr^{2+}.

Anti-interference ability is vital for the practical application of an extractant, and it was systematically evaluated in this study. The anti-interference performance of **Cu-MOF-COOH** nanosheets was first evaluated against these monovalent metal ions (Na^+, K^+, Rb^+, and Cs^+) by adding different metal ions into Sr^{2+} solution (5 ppm) with different ratios. The results shown in Fig. 3e demonstrated that the presence of single monovalent metal ions, with the same concentrations as Sr^{2+}, posed almost no effect on Sr^{2+} extraction, and the removal ratios for Sr^{2+} reached up to 99.45%, which is virtually equal to the removal ability for Sr^{2+} in the absence of interfering metal ions. Even when the concentrations of Na^+, K^+, and Cs^+ increased to 50 times that of Sr^{2+}, the extraction efficiency for Sr^{2+} remained almost unchanged, with a removal rate still exceeding 99%. For Rb^+, even with an elevated concentration of 250 ppm, 94.44% of Sr^{2+} can still be effectively removed.

The anti-interference performances toward divalent metal ions, specifically Mg^{2+}, Ca^{2+} and Ba^{2+}, were further investigated. Notably, the presence of Mg^{2+} exhibited negligible influence on Sr^{2+} removal, even at a high Mg^{2+}/Sr^{2+} ratio of 50, and **Cu-MOF-COOH** nanosheets demonstrated an ultra-high Sr^{2+} removal rate of 99.46% (Fig. 3e). For Ca^{2+} or Ba^{2+}, when their concentrations are equivalent to that of Sr^{2+}, the MOF nanosheets still retained effective removal, with Sr^{2+} removal efficiencies up to 92.48% and 91.16%, respectively (Fig. 3e). Even when the concentrations of Ca^{2+} and Ba^{2+} increased to 250 ppm, the removal efficiencies for Sr^{2+} remained at 71.18% and 66.00%, respectively. It should be noted that, although the MOF nanosheets exhibited a certain removal for Ba^{2+} (25.97%), the impact of Ba^{2+} on Sr^{2+} removal was not as substantial. In contrast, numerous studies have demonstrated that the presence of Ca^{2+} or Ba^{2+} significantly impeded Sr^{2+} removal. For instance, when Ca^{2+} was introduced into Sr^{2+} solution at the concentration that was 1 time (1-fold) of Sr^{2+}, the removal efficiency for Sr^{2+} by

potassium phosphatoantimonate (K_2SbPO_6) dropped drastically from the original 98.85% to 70.05%; when Ca^{2+} was introduced into Sr^{2+} solution at the concentration that was 50 times (50-fold) of Sr^{2+}, the removal efficiency for Sr^{2+} drops drastically to 25.94%.[47] Similarly, Ba^{2+} has also been shown to profoundly affect Sr^{2+} removal, as evidenced by a study on crown ether-based amino-modified mesoporous silica, where the removal efficiency for Sr^{2+} decreased significantly as the Ba^{2+}/Sr^{2+} molar ratio increased from 1 to 100.[48] The interference of Ca^{2+} and Ba^{2+} on Sr^{2+} removal is understandable because of their high proximity to Sr^{2+} in the periodic table and their shared chemical properties, which are known to be challenging to separate from Sr^{2+} in many circumstances.[49] Especially for Ca^{2+}, the high similarity to Sr^{2+} enables it to readily enter the body and substitute for calcium in bones, potentially leading to bone cancer.

In practical applications, Sr^{2+} often coexists with various competing metal ions. It is imperative to evaluate the anti-interference performance of **Cu-MOF-COOH** nanosheets in more complex environments. To this end, Sr^{2+} extraction performance was further assessed in the presence of mixed ions (Na^+, K^+, Rb^+, Cs^+, Mg^{2+}, Ca^{2+} and Ba^{2+}) with concentrations ranging from 5 to 100 ppm. The results shown in Fig. 3f demonstrated exceptional extraction performance for Sr^{2+}. Specifically, at a 1 : 1 concentration ratio of the mixed metal ions to Sr^{2+}, the removal rate for Sr^{2+} reached up to 94.53%. Even in the presence of 100 ppm mixed ions (the concentration ratio of mixed metal ions to Sr^{2+} is 20 : 1), the MOF nanosheets retained a removal ratio for Sr^{2+} of more than 76.35%, highlighting their remarkable anti-interference ability in the complex aqueous systems. In a similar simulated system, comprising five metal ions (Na^+, Mg^{2+}, K^+, Ca^{2+} and Ba^{2+}), where the concentration of these cations was 10 times higher than that of Sr^{2+}, the adsorbents of ZrP and CA@ZrP exhibited removal rates for Sr^{2+} of only 28% and 40.8%, respectively.[50] Meanwhile, the concentrations of competing ions in actual radioactive wastewater typically do not reach such high levels. Data from the elemental analysis report of a nuclear power plant's low-level radioactive wastes showed that the concentrations of the major elements (>1 ppm) of Na^+, Ca^{2+}, Mg^{2+}, and K^+, are 145 $\pm$ 5.8, 16.5 $\pm$ 2.4, 13.5 $\pm$ 3.1, and 92.3 $\pm$ 55.4 ppm, respectively.[51] These results suggested that the targeted Sr^{2+} capture by **Cu-MOF-COOH** nanosheets can be little affected by the presence of competing ions in practical scenarios.

The good selectivity and robust anti-interference abilities of **Cu-MOF-COOH** nanosheets motivated us to delve deeper into their performance in removing Sr^{2+} from actual water samples. Given the variability in the constituents and their concentration across diverse natural water bodies, the feasibility of employing MOF nanosheets for Sr^{2+} removal was evaluated in different water systems, including tap water, lake water, and simulated groundwater (Table 1 and Fig. S14†). The results shown in Table 1 demonstrated that the removal rate for Sr^{2+} reached an impressive value of 97.19% in simulated groundwater. Although the removal efficiency was slightly lower in tap water, MOF nanosheets still managed to remove 95.44% of Sr^{2+}. This observation may be attributed to the higher concentration of Ca^{2+} in tap water (33.45 ppm) compared to that in simulated groundwater (24.59 ppm), as outlined in Table 1. It is noteworthy that, even in lake water, which contains extensive competing ions and organic matrices, the removal rate for Sr^{2+} by MOF nanosheets still remained high, at 93.42%. To further assess the performance of MOF nanosheets under more challenging conditions, Sr^{2+} removal was evaluated in simulated radioactive wastewater, which includes extensive metal ions (Table 1). Remarkably, even in this highly complex system, the removal rate for Sr^{2+} still reached 91.04%. These results demonstrated the superior selectivity and anti-interference capabilities of the **Cu-MOF-COOH** nanosheet, making it a promising candidate for efficient Sr^{2+} separation in practical applications.

Extraction mechanism studies

To gain insights into the outstanding performance in Sr^{2+} separation, a series of characterization studies including PXRD, FT-IR, and X-ray photoelectron spectroscopy (XPS) were performed. As shown in Fig. S15,† the consistent PXRD patterns before and after Sr^{2+} extraction provided evidence for the robust structural stability of **Cu-MOF-COOH** nanosheets. In the FT-IR spectrum (Fig. S16†), a new peak that appeared at 740 cm^{-1} after extraction is attributed to the stretching vibration of the Sr–O bond, confirming the successful loading of Sr^{2+} onto the nanosheets.[52] After Sr^{2+} extraction, the peaks of the asymmetric and symmetric vibrational modes of COO^- shifted from 1616 and 1413 cm^{-1} to 1613 and 1419 cm^{-1}, respectively, demonstrating the coordination interactions between Sr^{2+} and carboxylate groups.[53,54] XPS spectra were further employed to provide more information on the interactions between MOF nanosheets and Sr^{2+}. For **Cu-MOF-COOH** nanosheets before and after Sr^{2+} extraction, all the characteristic peaks of C 1s, O 1s, and Cu 2p can be observed in their XPS survey spectra (Fig. 4a). A unique peak of Sr 3d only appeared in the spectrum of **Cu-MOF-COOH** nanosheets after extraction, which directly confirmed Sr^{2+} extraction by MOF nanosheets (Fig. 4a). The high-resolution spectrum of Sr 3d can be divided into peaks at 135.69 eV and 133.87 eV (Fig. 4b), corresponding to the characteristic peaks of Sr $3d_{3/2}$ and Sr $3d_{5/2}$, respectively.[55] These peaks showed an obvious shift towards lower binding energies in comparison to those of original $Sr(NO_3)_2$, which were located at 136.18 eV (for Sr $3d_{3/2}$) and 134.48 eV (for Sr $3d_{5/2}$),[50] indicating the interactions between Sr^{2+} with the MOF nanosheets. Following Sr^{2+} extraction, the peaks of C–O and C=O in the high-resolution spectrum of O 1s (Fig. 4c) exhibited a shift from 533.53 and 532.62 eV to 533.66 and 532.84 eV, respectively, which can be stemmed from the interactions between Sr^{2+} and the oxygen-containing functional groups that induce the alteration in the electronic environment of the oxygen atoms.[8] The novel peak appeared at 532.06 eV after Sr^{2+} extraction is attributed to Sr–O binding, providing further evidence for the interactions between Sr^{2+} and the oxygen element. Combined with FT-IR analysis, these obvious changes of binding energies in XPS spectra demonstrated a strong affinity between Sr^{2+} and the carboxylate groups in MOF nanosheets.

Table 1 Sr^{2+} capture performance from various water samples (with spiked Sr^{2+}) by **Cu-MOF-COOH** nanosheets

Water samples	Coexisting ion concentrations (ppm)	Sr^{2+} initial concentration (ppm)	Sr^{2+} removal rate
Contaminated tap water	Na^+ (7.12) K^+ (6.87) Mg^{2+} (9.19) Ca^{2+} (33.45)	5.14	95.44%
Contaminated lake water	Na^+ (6.91) K^+ (6.66) Mg^{2+} (8.08) Ca^{2+} (29.57)	5.25	93.42%
Contaminated simulated groundwater	Na^+ (125.35) K^+ (6.25) Mg^{2+} (9.79) Ca^{2+} (24.59)	5.34	97.19%
Simulated low-level radioactive wastewater	Al^{3+} (0.01) Mo^{3+} (4.85) Cu^{2+} (0.04) Mg^{2+} (1.10) Pb^{2+} (0.07) Zn^{2+} (0.06) Cs^+ (6.61) Mn^{2+} (3.40) Fe^{2+} (3.21) Ca^{2+} (2.01) Rb^+ (3.57)	4.45	91.04%

Theoretical model calculations were performed to gain a deep understanding of the interactions between **Cu-MOF-COOH** nanosheets and Sr^{2+} at the molecular level. Based on the crystal structure of **Cu-MOF-COOH** and analysis of FT-IR and XPS studies, we selected the cage-like cavity unit (Fig. S2†) as a model for theoretical calculations, and the uncoordinated carboxylate oxygen atoms within the cavities as potential binding sites. Typically, Sr^{2+} adopts 8- to 9-coordinate geometries in aqueous or framework environments. Thus, the constructed theoretical model would account not only for the potential binding of carboxylate sites but also for the inclusion of terminal water ligands to achieve the typical 8-coordinate geometry for Sr^{2+} in aqueous environments. Initially, a simple model was constructed, in which each Sr^{2+} was mono-coordinated with an oxygen atom from a carboxylate group and seven-coordinated with seven water molecules (Fig. 5a). The binding energy (E_b) for this model was calculated to be −1.68 eV (model I). To identify more energetically favored extraction modes, more complex coordination modes with carboxylate groups were constructed (Fig. 5b–f), including bridging mode (model II) and chelation mode (model III). In model II, Sr^{2+} was coordinated by two oxygen atoms from two different carboxylate groups and six oxygen atoms from six water molecules (model II-a and model II-b; Fig. 5b and c). Compared to model I, these models in model II didn't show a significant decrease in the binding energies (−1.50 and −1.82 eV), suggesting that bridging coordination isn't the optimal coordination model. In chelation modes, Sr^{2+} formed a single chelate ring by coordinating with two oxygen atoms from one carboxylate group (model III-a, $E_b = -2.17$ eV; Fig. 5d), and it can also be chelated by two carboxylate groups at *ortho*-positions (model III-b and III-c, $E_b = -2.69$ and −2.95 eV; Fig. 5e and f), forming a dual-ring structure. By comparing these binding energies, the chelation models (model III-a, III-b and III-c; Fig. 5d–f) exhibit much lower values than those of other models. In particular, the double carboxylate chelation in model III-c provides the most energetically favorable and stable configuration among all the constructed models, highlighting the critical role of carboxylate groups in the selective capture of Sr^{2+}.

The H_4L ligand, characterized by four carboxyl groups, holds intriguing potential for Sr^{2+} extraction. To assess its binding ability for Sr^{2+} capture, theoretical calculations were utilized to model the extraction process and calculate the molecular-level binding energy of the ligand towards Sr^{2+} (Fig. S17†). In the mono-coordinated mode, Sr^{2+} interacted with one oxygen atom within a carboxylate group and seven water molecules, yielding a binding energy of −0.56 eV (Fig. S17a†). In the bridging interaction mode, Sr^{2+} coordinated with two carboxylate groups and six water molecules, resulting in a binding energy of −1.07 eV (Fig. S17b†). In the chelate mode, Sr^{2+} could form either a single chelate ring (−1.18 eV) with one carboxylate group or a dual-ring structure (−1.95 eV) by chelating two

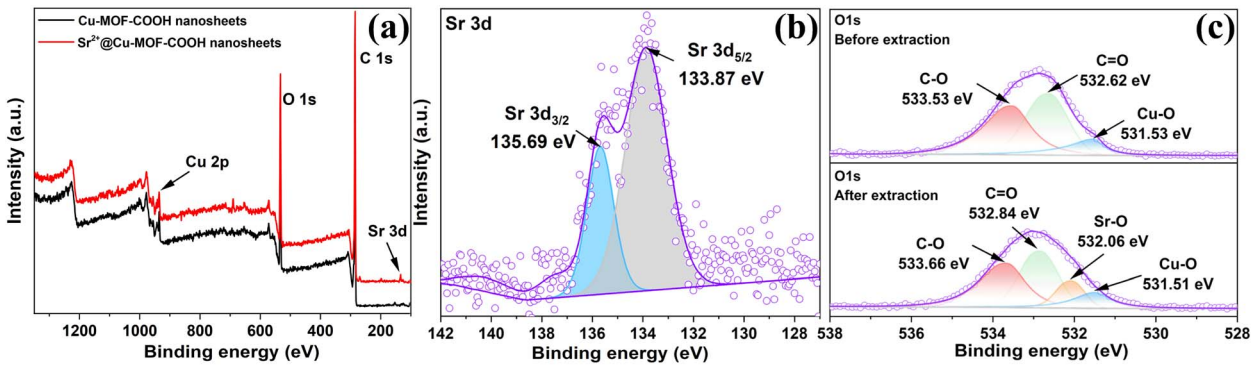

Fig. 4 (a) XPS survey spectrum of **Cu-MOF-COOH** nanosheets (contrast of Sr^{2+} extraction). (b) High-resolution XPS spectra of Sr 3d (after Sr^{2+} extraction) and (c) O 1s (before and after Sr^{2+} extraction).

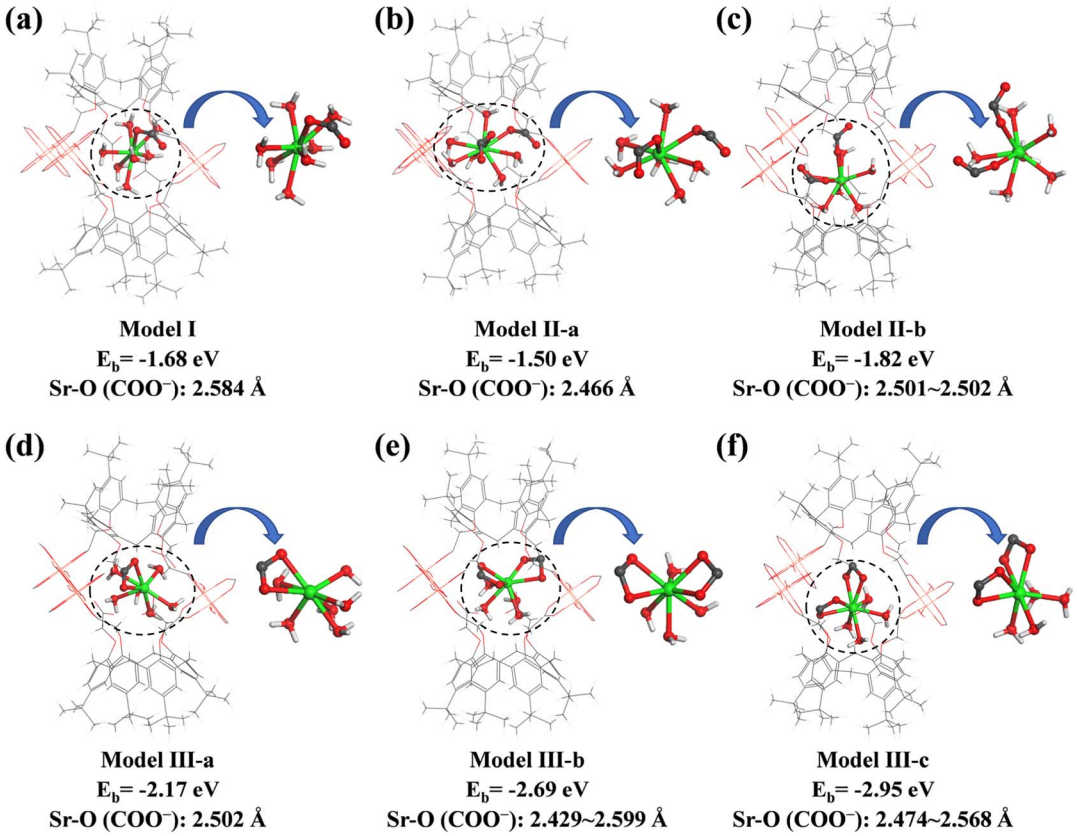

Fig. 5 (a–f) Model calculations for Sr^{2+} capture.

carboxylate groups (Fig. S17c and d†). By comparing these binding energies, the double carboxylate chelation model emerged as the most energetically favorable configuration among all the constructed models. This result is in line with our expectations and consistent with the previous observations for **Cu-MOF-COOH** nanosheets. These models of the H_4L ligand exhibit much higher binding energies compared to those observed in **Cu-MOF-COOH** nanosheets (−2.95 eV), which suggests that the binding affinity with Sr^{2+} is inferior to that of MOF nanosheets. These theoretical results are consistent with the experimental observations that the extraction selectivity of the H_4L ligand is obviously lower than that of **Cu-MOF-COOH** nanosheets (Fig. 3d).

The good selectivity of MOF nanosheets toward Sr^{2+} can stem from the synergistic interaction between the carboxylate groups and the cage-like cavities with Sr^{2+}. To elucidate the role of the cage-like cavities in Sr^{2+} extraction, we constructed another model (Fig. S18†) that was similar to the optimal mode (model III-c; Fig. 5f) but without the cage-like cavities. The calculated E_b value for this model (−1.34 eV) is significantly higher than the E_b observed in **Cu-MOF-COOH** nanosheets (−2.95 eV), which indicates that the absence of the cage-like cavities is unfavorable for the synergistic interaction with Sr^{2+}, resulting in a substantial reduction in the interaction strength. These results demonstrated that the presence of the cage-like cavity is crucial for enhancing the binding strength and selectivity toward Sr^{2+}. In particular, the synergistic interaction between the cage-like cavity and the carboxylate groups with Sr^{2+} provides an optimized spatial confinement and a specific coordination environment for Sr^{2+}, thereby playing a pivotal role in the selective capture of Sr^{2+}.

Furthermore, to confirm the high selectivity of MOF nanosheets toward Sr^{2+}, we calculated the binding energies for various metal ions. As shown in Fig. S19,† MOF nanosheets exhibited the lowest binding energy for Sr^{2+} (−2.95 eV), followed by Ba^{2+} (−2.49 eV), Ca^{2+} (−1.66 eV) and Mg^{2+} (−1.59 eV), while the binding energies towards alkali metal ions are significantly higher, indicating the strongest interactions with Sr^{2+}. This result aligns with previous experimental results, providing robust evidence for the exceptional affinity and selectivity of **Cu-MOF-COOH** nanosheets for Sr^{2+}.

Reusability of Cu-MOF-COOH nanosheets

The regeneration and recyclability of MOF nanosheets are crucial for assessing their economic viability in wastewater treatment. A detailed investigation into the reusability of MOF nanosheets was conducted by using 0.01 M Na_2HPO_4 solution as an eluent. The results shown in Fig. S20† demonstrated fair regeneration ability of **Cu-MOF-COOH** nanosheets. Specifically, the extraction rate experienced a minimal decline of 0.43% in the initial cycle, and the MOF nanosheets still retained a high removal rate of 87.95% even after five cycles. The gradual decrement in extraction capacity can be attributed to the

occupation of binding sites by the residual Sr^{2+}. Furthermore, the concentrations of Cu^{2+} in the toluene phase and aqueous phase were determined after Sr^{2+} extraction to calculate the Cu^{2+} leaching rate. Through the inductively coupled plasma mass spectrometry measurement, only 0.24% and 0.13% of Cu^{2+} were determined in the toluene phase and aqueous phase (Table S1†), respectively, which demonstrated the good chemical stability of **Cu-MOF-COOH** nanosheets. The PXRD result further evidenced the retained crystallinity and structural stability of the MOF nanosheets after regeneration tests (Fig. S21†), indicating their fair reproducibility.

Conclusions

In conclusion, an ultrathin 2D **Cu-MOF-COOH** nanosheet with a cavity structure was elaborately fabricated. The as-synthesized MOF nanosheets showed a high uptake capacity (231.72 mg g^{-1}) for Sr^{2+}, which is much higher than that of most other materials, including 3D **Cu-MOF-COOH** (147.79 mg g^{-1}). The MOF nanosheets exhibited exceptional selectivity for Sr^{2+} and a robust resistance to interference, even when exposed to high concentrations of competing ions such as Ca^{2+}, Ba^{2+}, and other alkali and alkaline-earth metals. The outstanding performance was further verified by their ability to efficiently remove over 91% of Sr^{2+} from a range of water samples, including lake water, simulated groundwater, and radioactive wastewater. The synergistic interactions between the carboxylate groups and the cage-like cavities with Sr^{2+} can account for the exceptional extraction performance for Sr^{2+}, which has been systematically investigated and clarified by detailed characterization studies and theoretical calculations. Compared to their 3D counterparts, **Cu-MOF-COOH** nanosheets exhibited obviously better extraction performance due to their highly open structure, which effectively exposes their surface active sites, facilitating intimate contact and comprehensive interactions with Sr^{2+} in the cage-like cavities.

Data availability

The data supporting this article have been included as part of the ESI.†

Author contributions

X.-R. Jia: investigation, methodology, conceptualization, writing-original draft. Z.-X. Gao: investigation, validation. H.-M. Fei: writing-original draft. L.-J. Lan: resources. C.-X. Yu: conceptualization, funding acquisition, methodology, writing-original draft. Y. Qian: resources, supervision, funding acquisition. L.-L. Liu: conceptualization, project administration, supervision, funding acquisition, writing-review & editing.

Conflicts of interest

There are no conflicts to declare.

Acknowledgements

This work was supported by the National Natural Science Foundation of China (No. 42407657 and 22466002), the Natural Science Foundation of Shandong Province (No. ZR2021MB106 and ZR2021QB090), the Training Program for Academic and Technical Leaders of Major Disciplines of Jiangxi Province (No. 20225BCJ22008) and the Natural Science Foundation of Jiangxi Province (No. 20242BAB26061).

References

1 W. Wu, D. Chen, M. Zhang, X. Zhao, R. Zhao, C. Geng, J. Jia and G. Zhu, *J. Am. Chem. Soc.*, 2025, **147**, 2228–2236.
2 Y.-M. Zhao, L. Cheng, K.-Y. Wang, X. Hao, J. Wang, J.-Y. Zhu, M. Sun and C. Wang, *Adv. Funct. Mater.*, 2022, **32**, 2112717.
3 Y. Kim, K. Jin, I.-H. Park, S. Lee, J. Park and J. Park, *Chem. Eng. J.*, 2024, **484**, 149321.
4 H.-Y. Sun, B. Hu, T.-T. Lv, Y.-L. Guo, Y.-X. Yao, L. Yang, M.-L. Feng and X.-Y. Huang, *Small*, 2023, **19**, 2208212.
5 N. Yang, X. Guo, J. Yu, Q. Liu, J. Liu, J. Zhu, R. Chen and J. Wang, *J. Hazard. Mater.*, 2025, **485**, 136955.
6 S. G. Lim, C. Y. Oh, S. H. Kim, K. Ra, M. Cha and J.-H. Yoon, *Environ. Sci. Technol.*, 2024, **58**, 6170–6180.
7 X. Du, H. Xie, T. Qin, Y. Yuan and N. Wang, *Nat. Commun.*, 2024, **15**, 6530.
8 L. Li, K. Kang, T.-S. Chee, Z. Tian, Q. Sun and C. Xiao, *Adv. Sci.*, 2024, **11**, 2308663.
9 H. Taketomi, N. Hosono and T. Uemura, *J. Am. Chem. Soc.*, 2024, **146**, 16369–16374.
10 K. Geng, Y. Sun, Y. Zhao, Z. Shao, Y. Wei, J. Huang, Y. Cui, X. Xu and H. Hou, *J. Am. Chem. Soc.*, 2025, **147**, 9844.
11 L. Xiao, C. Cheng, Z. Li, C. Zheng, J. Du, M. Song, Y. Wan, S. Li, G. Jun and M. Zhao, *Nano Res.*, 2023, **16**, 11334–11341.
12 S. Yang, Y. Sun, K. Geng, Y. Cui, J. Huang, X. Meng and H. Hou, *Adv. Opt. Mater.*, 2024, **12**, 2400475.
13 S.-H. Zhou, R.-D. Wang, Y. Yang, H.-Y. Li, L.-J. Luo and F.-Z. Jiang, *J. Clean. Prod.*, 2024, **476**, 143807.
14 J. Zhang, L. Chen, X. Dai, L. Zhu, C. Xiao, L. Xu, Z. Zhang, E. V. Alekseev, Y. Wang, C. Zhang, H. Zhang, Y. Wang, J. Diwu, Z. Chai and S. Wang, *Chem*, 2019, **5**, 977–994.
15 Y. Qin, J. Du, Q. Zhang, C. Cheng, Z. Dong, Q. Zhang, S. Li, J. Guo, Z. Tang and M. Zhao, *Adv. Mater.*, 2025, **37**, 2419515.
16 D. Guo, C. Yan, B. Huang, T. Jin, Z. Liu and Y. Qian, *Inorg. Chem.*, 2025, **64**, 1777–1787.
17 S. Deng, X. Kong, X. Fu, Z.-W. Huang, Z.-H. Zhou, L. Mei, J.-P. Yu, L.-Y. Yuan, Y.-Q. Zhu, N.-N. Wang, K.-Q. Hu and W.-Q. Shi, *Inorg. Chem.*, 2025, **64**, 224–231.
18 L. González, R. Gil-San-Millán, J. A. R. Navarro, C. R. Maldonado, E. Barea and F. J. Carmona, *J. Mater. Chem. A*, 2022, **10**, 19606–19611.
19 X. Zhao, X. Gao, R. Ding, H. Huang, X. Gao and B. Liu, *J. Colloid Interface Sci.*, 2023, **639**, 59–67.
20 Y. Wang, D. Ren, J. Ye, Q. Li, D. Yang, D. Wu, J. Zhao and Y. Zou, *Sep. Purif. Technol.*, 2024, **329**, 125149.
21 Y. Qing, W. Gao, Y. Long, Y. Kang and C. Xu, *Inorg. Chem.*, 2023, **62**, 6909–6919.

22 M.-R. Yao, H. Wu, C.-X. Yu, J. Ding, Y.-L. Zhou and L.-L. Liu, *Sep. Purif. Technol.*, 2025, **360**, 131048.
23 C.-X. Yu, W. Jiang, M. Lei, M.-R. Yao, X.-Q. Sun, Y. Wang, W. Liu and L.-L. Liu, *Small*, 2024, **20**, 2308910.
24 K. Jin, B. Lee and J. Park, *Coord. Chem. Rev.*, 2021, **427**, 213473.
25 R.-J. Cao, H.-Y. Zhou, Q.-Y. Wu, Z. Xiao, T.-Y. Xiu, J. Li, H.-B. Tang, L.-Y. Yuan, W.-S. Wu and W.-Q. Shi, *Adv. Mater.*, 2025, **37**, 2414659.
26 Q. Peng, B. Huang, L. Peng, D. Guo, T. Jin, Z. Liu and Y. Qian, *Sep. Purif. Technol.*, 2024, **337**, 126391.
27 L. Feng, X. Chen, M. Cao, S. Zhao, H. Wang, D. Chen, Y. Ma, T. Liu, N. Wang and Y. Yuan, *Angew. Chem., Int. Ed.*, 2023, **62**, e202312894.
28 W. Jin, Q. Wu, Y. Lou, Z. Huang, F. Liu, B. Hu, J. Yu, K. Hu, L. Yuan, W. Shi and L. Mei, *Sci. Bull.*, 2025, **70**, 683–693.
29 G. Lin, B. Zeng, X. Liu, J. Li, B. Zhang and L. Zhang, *J. Clean. Prod.*, 2022, **381**, 134766.
30 B. Han and A. Chakraborty, *Desalination*, 2022, **541**, 116045.
31 X. Chen, W. Wang, Y. Song, Y. Zhou, H. Li and J. Pan, *J. Hazard. Mater.*, 2022, **438**, 129522.
32 R. Liu, Q. Zhao, Z. Wang, R. Jiang, C. Lin, L. Wu, G. Chen, P. He, L. Zhu, J. Chen and T. Duan, *J. Mater. Chem. A*, 2024, **12**, 14608–14618.
33 M.-R. Yao, Z.-Y. Wang, A.-C. Geng, K.-Y. Wu, M.-J. Luo, Z.-H. Li, Y.-Q. Sun, M.-J. Gao, C.-X. Yu and L.-L. Liu, *Sep. Purif. Technol.*, 2024, **341**, 126892.
34 H. Sun, K.-Z. Wang, M.-R. Yao, C.-X. Yu, Y.-H. Song, J. Ding, Y.-L. Zhou, D. Liu and L.-L. Liu, *Inorg. Chem. Front.*, 2023, **10**, 6566–6577.
35 J. Yu, J. Wang, H. Zhang, Q. Liu, J. Liu, J. Zhu, J. Yu and R. Chen, *Carbohydr. Polym.*, 2024, **323**, 121426.
36 J.-Y. Tian, W.-C. Lv, A.-S. Shen, Y. Ma, M. Wang, S. Zhang, X.-L. Liu, Z. Zhang and M. Du, *Sep. Purif. Technol.*, 2023, **327**, 124903.
37 T. Prakasam, S. K. Sharma, F. Ravaux, F. Benyettou, M. Lusi, V. Sabu, P. Bazin, T. Delclos, R. Jagannathan, J. Whelan, M. El-Roz, M. A. Olson, M. Abdellatief, O. S. Mudraj, F. Gándara and A. Trabolsi, *Chem*, 2025, **11**, 102307.
38 L.-L. Liu, J. Chen, Y. Zhang, C.-X. Yu, W. Du, X.-Q. Sun, J.-L. Zhang, F.-L. Hu, Y. Mi and L.-F. Ma, *J. Mater. Chem. A*, 2021, **9**, 546–555.
39 C.-X. Yu, W. Jiang, C.-W. Zhang, H. Fang, L.-Z. Wang, M.-J. Gao, Y.-L. Zhou, Y. Qian and L.-L. Liu, *Inorg. Chem.*, 2024, **63**, 15105–15114.
40 B. Garai, D. Shetty, T. Skorjanc, F. Gándara, N. Naleem, S. Varghese, S. K. Sharma, M. Baias, R. Jagannathan, M. A. Olson, S. Kirmizialtin and A. Trabolsi, *J. Am. Chem. Soc.*, 2021, **143**, 3407–3415.
41 T. Skorjanc, D. Shetty, F. Gándara, S. Pascal, N. Naleem, S. Abubakar, L. Ali, A. K. Mohammed, J. Raya, S. Kirmizialtin, O. Siri and A. Trabolsi, *ACS Appl. Mater. Interfaces*, 2022, **14**, 39293–39298.
42 L.-D. Yu, Y.-J. Tong, N. Li, Y. Yang, P. Ye, G. Ouyang and F. Zhu, *Chem. Commun.*, 2022, **58**, 11697–11700.
43 P. Yang, J. Jiang, J.-P. Ma, B. Zheng, Y. Yan, J. Wang, Y. Zou, Q.-K. Liu and Y. Chen, *Inorg. Chem.*, 2022, **61**, 1521–1529.
44 Z. Li, K. Li, Y. Li, Y. Yu, J. Lv, X. Liu, K. Guan, W. Lei, S. Zhang and H. Zhang, *Adv. Funct. Mater.*, 2024, **34**, 2310371.
45 L.-J. Ji, T.-Y. Yang, G.-Q. Feng, S. Li, W. Li and X.-H. Bu, *Adv. Mater.*, 2024, **36**, 2404756.
46 Y. Wang, W. Zhang, X. Zeng, T. Deng and J. Wang, *Sep. Purif. Technol.*, 2021, **278**, 119640.
47 Y.-L. Guo, H.-Y. Sun, X. Zeng, T.-T. Lv, Y.-X. Yao, T.-H. Zhuang, M.-L. Feng and X.-Y. Huang, *Chem. Eng. J.*, 2023, **460**, 141697.
48 R. I. Ripon, Z. A. Begum, B. Ahmmad, F. Hirose, Y. Takagai and I. M. M. Rahman, *J. Environ. Chem. Eng.*, 2024, **12**, 113984.
49 X. Zhang and Y. Liu, *J. Hazard. Mater.*, 2020, **398**, 122907.
50 R. Liu, G. Chen, Z. Wang, Q. Zhao, L. Wu, Q. Li, R. Tian, X. Chen, X. Li, Z. Chen, L. Zhu, J. Chen and T. Duan, *Inorg. Chem.*, 2023, **62**, 5799–5809.
51 I. B. Rae, S. Pap, D. Svobodova and S. W. Gibb, *Sci. Total Environ.*, 2019, **650**, 2411–2422.
52 Q. Li, X. Wang, L. Song, L. He, Q. Yu, X. Xiao and S. Ding, *J. Environ. Chem. Eng.*, 2023, **11**, 110495.
53 R. Paz, H. Viltres, N. K. Gupta, C. Leyva, R. P. Dhavale, H.-H. Park, A. Romero-Galarza, A. R. Rajabzadeh and S. Srinivasan, *J. Environ. Chem. Eng.*, 2023, **11**, 110084.
54 R. Paz, N. K. Gupta, H. Viltres, C. Leyva, A. Romero-Galarza, S. Srinivasan and A. R. Rajabzadeh, *Sep. Purif. Technol.*, 2022, **298**, 121606.
55 J. Diao, J. Zu, G. Han, Y. Xue, X. Pan, M. Jin, S. Liu and Q. Tang, *Sep. Purif. Technol.*, 2023, **325**, 124644.